Structural characterization of off-stoichiometric kesterite-type $Cu_2ZnGeSe_4$ compound semiconductors: From cation distribution to intrinsic point defect density

René Gunder[1], Jose Márquez-Prieto[1], Galina Gurieva[1], Thomas Unold[1] and Susan Schorr[1,2]

[1]Helmholtz-Zentrum Berlin für Materialien und Energie GmbH, Department Structure and Dynamics of Energy Materials, Hahn-Meitner-Platz 1, D-14109 Berlin, Germany

[2]Freie Universität Berlin, Institut für Geologische Wissenschaften, Malteserstr. 74-100, D-12249 Berlin, Germany

Keywords

Kesterite-type compound, X-ray powder diffraction, WDX spectroscopy, neutron powder diffraction, Rietveld method, point defects, diffuse reflectance, bandgap energy, hyperspectral imaging

Abstract

The substitution of Ge^{4+} for Sn^{4+} in $Cu_2ZnSn(S,Se)_4$ (CZTSSe) kesterite-type absorber layers for thin film solar cells has proven to enhance the opto-electronic properties of the material. By cationic substitution, in general, the optical bandgap can be more readily designed for the purpose of bandgap engineering, and the substitution of Sn^{4+} by Ge^{4+}, in particular, widens the optical bandgap such that it can be employed both for photovoltaics as well as solar fuel quarrying by photocatalytic water splitting. This work is an experimental study of intrinsic point defects in off-stoichiometric kesterite-type $Cu_2ZnGeSe_4$ (CZGSe) by means of neutron powder diffraction. We revealed the existence of copper vacancies (V_{Cu}), various cation antisite defects (Cu_{Zn}, Zn_{Cu}, Zn_{Ge}, Cu_{Ge}) as well as interstitials (Cu_i, Zn_i) in a wide range of off-stoichiometric polycrystalline material synthesized by solid state reaction. In addition to the off-stoichiometry type specific defects, Cu/Zn disorder is always present in the kesterite-type CZGSe phase. While compositional changes are clearly reflected by the tetragonal deformation *c/2a*, the lattice parameters *a*, *c* seem differently responding to point defect types and concentration variations, respectively. The Cu_{Ge} antisite defect which is known to greatly deteriorate the opto-electronic properties exists only in Cu-rich CZGSe, but appears already in CZGSe with Cu/(Zn+Ge)≈1. Furthermore we showed by diffuse reflectance hyperspectral imaging a widening of the energy bandgap in off-stoichiometric kesterite-type CZGSe with decreasing Cu/(Zn+Ge).

Introduction

Since the late 1970s [1] quaternary chalcogenides like $Cu_2ZnSn(S,Se)_4$ kesterite-type compounds were known to be intrinsic semiconductors possessing a direct optical bandgap suitable for being used as solar energy converter. However, ternary chalcopyrite-type compounds have been one of the first chalcogenide materials to be considered as absorber layer in 2nd generation solar cells based on thin film technology [2], likely due to lower complexity in terms of phase relations and structural properties. And yet, kesterite-type compounds started to be increasingly studied as absorber layer in thin film solar cells [3, 4] and more efforts were put into improving power conversion efficiencies which, so far, culminates in 12.6 % record efficiency [5]. In spite of the still superior performance of thin film solar cells based on chalcopyrite-type absorbers it has been realized that upscaling from laboratory process to GW production (and beyond) might be not feasible as the deployment of the trivalent cations In^{3+} and Ga^{3+} in $A^I B^{III} X_2^{VI}$ [6] chalcopyrite-type compound semiconductors are expected to cause future shortage and, correspondingly, goes along with a high risk of cost increase. So for the purpose of upscaling, the barrier of availability has to be overcome by considering materials consisting of abundant elements. With $A_2^I B^{II} C^{IV} X_4^{VI}$ kesterite-type compound semiconductors the possibility is more likely given for large scale production of potentially low cost and high efficiency solar cells. However, one has to be aware of the fact that substituting Sn^{4+} for Ge^{4+}, of course, does counteract the philosophy of avoiding deployment of rather rare elements. Nevertheless, it was demonstrated that CZTSe absorber layers doped with Ge show improved V_{OC} along with enhanced grain growth [7] as well as improved voltage dependent charge carrier collection [8]. Ultimately, the exploitation of solar energy for photovoltaics as well as solar fuels production also features a promising future prospect.

Kesterite-type materials belong to the adamantine compound family [9] and crystallize in the tetragonal crystal system with a body-centred unit cell and a four-fold rotational inversion along the c-axis, resulting in space group $I\bar{4}$ [10-12]. In the kesterite-type structure five Wyckoff positions are occupied. The 2a and 2c positions are occupied by a univalent cation (e.g. Cu^+) while the divalent cation (e.g. Zn^{2+}) is accommodated by the 2d position, and the tetravalent cation (e.g. Sn^{4+}, Ge^{4+}) is occupying the 2b position. Because of this cationic arrangement the anion located at the 8g position is shifted off the centre of the cation tetrahedron (Figure 1a). The aforementioned cation positions, though, only hold for perfectly ordered kesterite, where the 2c and 2d position at z=0.25 and z=0.75 would be fully occupied by copper and zinc, respectively. The kesterite-type semiconductors Cu_2ZnSnS_4 and $Cu_2ZnSnSe_4$, however, exhibit an order-disorder transition [13] at critical temperature T_c. Above the critical temperature the crystal can be described to be in dynamic equilibrium, with copper and zinc being readily interchanged since energy differences between 2c and 2d sites are small [13, 14]. As temperature falls below T_c copper and zinc start to order on their respective positions. Therefore disorder decreases with decreasing temperature and tends to approach the completely ordered state if temperature is sufficiently low and equilibration time (i.e. cooling rate) is sufficiently long. This, however, is normally not realized since equilibration times are usually well below of what would be required [15], and it has been demonstrated that the Cu/Zn disorder in CZTSe is influenced both by the extent as well as direction of off-stoichiometry too [16]. Hence kesterite-type materials are considered to always show a certain amount of Cu/Zn disorder [16] (Figure 1b) which is supposed to be an essential source for bandgap fluctuation [17, 18] and, eventually, contributes to the V_{oc} deficit [19, 20] of kesterite-based solar cells.

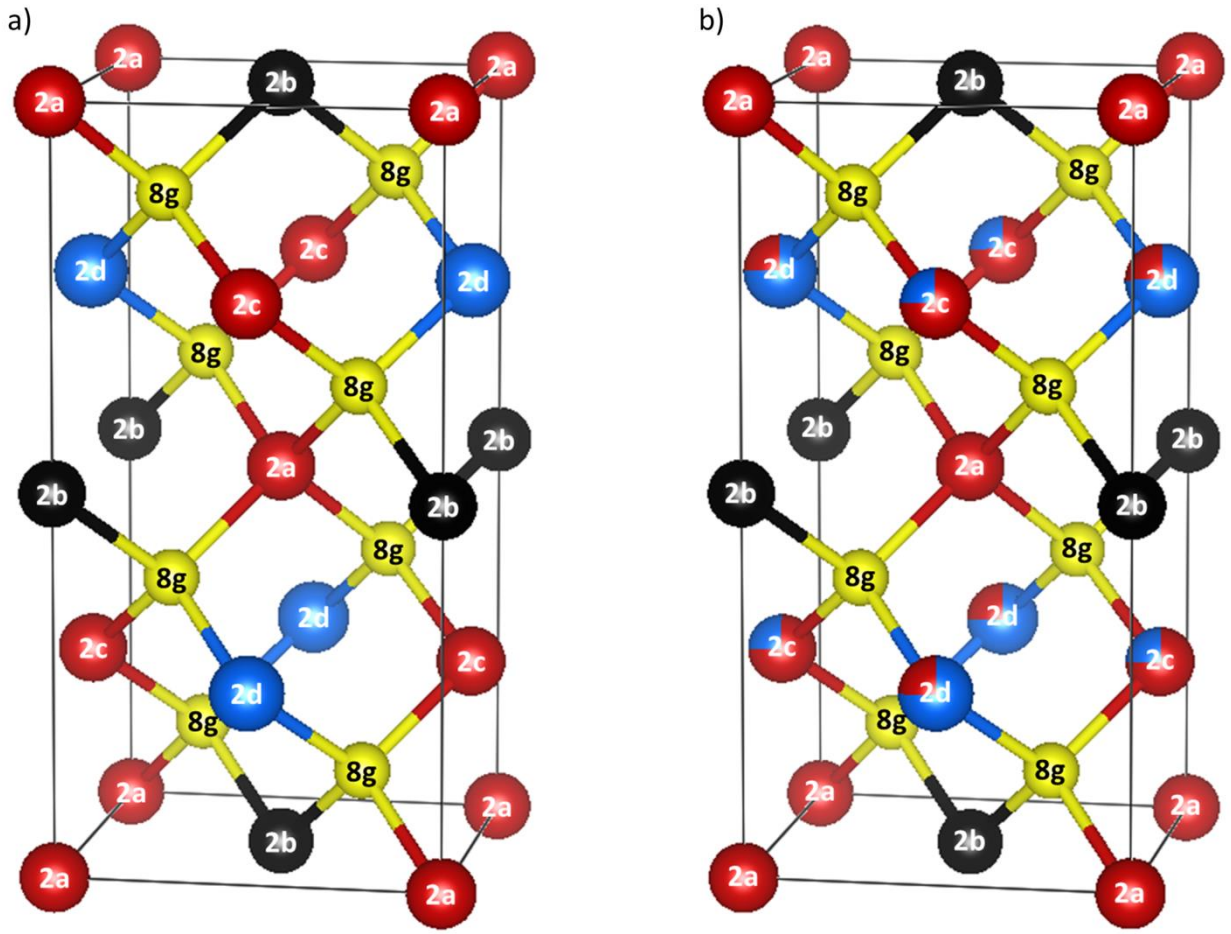

Figure 1. Representation of the unit cell of the kesterite structure (space group $I\bar{4}$) [10-12]. a) ordered kesterite, b) 50% disordered kesterite. Copper is depicted in red, zinc in blue, germanium in black and selenium in yellow.

Most chalcogenide materials exhibit p-type conductivity while, for instance, $Ag_2ZnSn(S,Se)_4$ is known to show n-type conductivity [21]. One advantage of chalcogenides in general and, particularly of kesterite-type compounds, is the high chemical variability allowing for readily adjustment of the bandgap energy. This flexibility in designing the bandgap energy is of great benefit for optimizing band alignments at heterojunction interfaces and minimizing recombination in the solar cells through chemical gradients [22]. Another advantage linked to this issue is the possibility to harvest sunlight not only for the purpose of photovoltaics but also for hydrogen production by photocatalytic water splitting. While 1.23 eV is the minimum energy required for water splitting it has been reported that bandgap energies around 2 eV turned out to provide the best energy conversion and highest quantum efficiencies [23]. In the solid solution CZTSe – CZTS cationic substitution of Sn^{4+} for Ge^{4+} widens the bandgap energy from about 1.0 (CZTSe) – 1.5 (CZTS) eV [24] to about 1.5 (CZGSe) – 2.2 (CZGS) eV [25], respectively. Hence, this range of higher bandgap energy is more suited in terms of solar energy conversion into chemical energy (i.e. hydrogen production) whilst being less capable of reaching highest photovoltaic performance. For photovoltaic applications, eventually, the best performing solar cells could be achieved with an optical bandgap energy of 1.34 eV [26] according to the Shockley-Queisser limit, and by using off-stoichiometric kesterite-type absorbers, in which the overall composition of the films is Cu-poor and Zn-rich [27, 28]. The

deviation from stoichiometry has been systematized according to certain cation substitution processes forming defect complexes. Considering the possible cation substitution reactions maintaining charge balance, 12 different off-stoichiometry types (A – L) can be established [16, 29-31]. The off-stoichiometry types and the corresponding intrinsic point defects of kesterite-type compounds are schematized in Figure 2 and summarized in Table I.

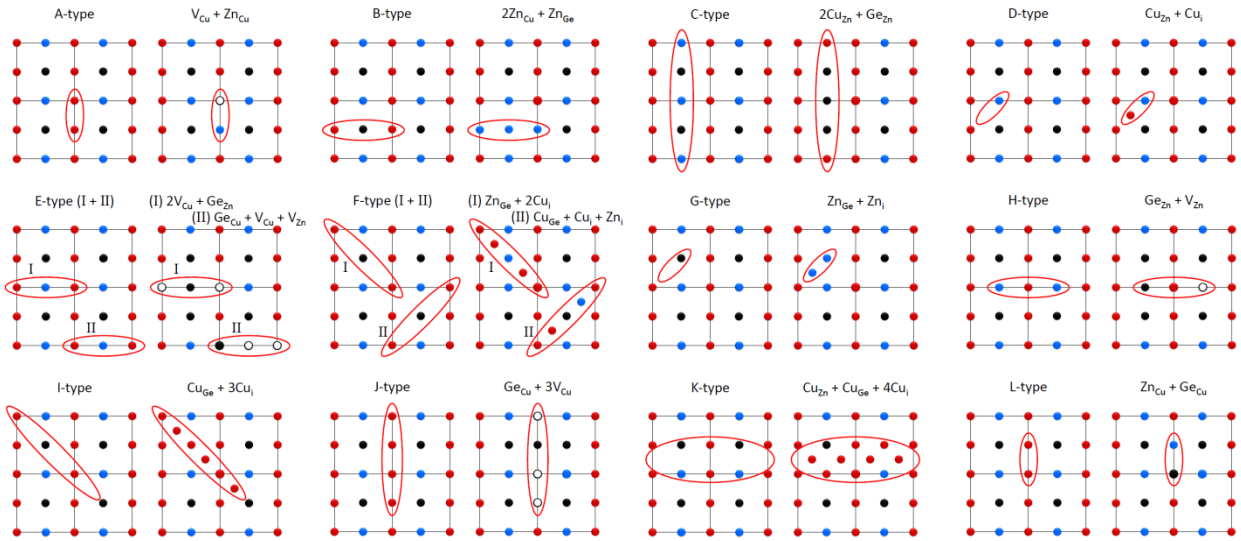

Figure 2. Schematic of unit cells along [001] direction showing cation planes at z=0 and z=0.25 to illustrate cation substitution processes and corresponding A-, B-, C- and D-type [29], E- and F-type [30], G-, H-type [31] and I-, J-, K- and L-type point defects. For better visibility four unit cells are shown and anions have been excluded. (Extended and modified after [30])

Table I. Overview of off-stoichiometry types in kesterite-type compounds.

type	composition	cation substitution reaction	intrinsic point defect	chemical formulae
A	Cu-poor, Zn-rich, Ge-const.	$2Cu^+ \rightarrow Zn^{2+}$	$V_{Cu} + Zn^{2+}_{Cu}$	$Cu_{2-2a}Zn_{1+a}GeSe_4$
B	Cu-poor, Zn-rich, Ge-poor	$2Cu^+ + Ge^{4+} \rightarrow 3Zn^{2+}$	$2Zn^{2+}_{Cu} + Zn^{2+}_{Ge}$	$Cu_{2-2b}Zn_{1+3b}Ge_{1-b}Se_4$
C	Cu-rich, Zn-poor, Ge-rich	$3Zn^{2+} \rightarrow 2Cu^+ + Ge^{4+}$	$2Cu^+_{Zn} + Ge^{4+}_{Zn}$	$Cu_{2+2c}Zn_{1-3c}Ge_{1+c}Se_4$
D	Cu-rich, Zn-poor, Ge-const.	$Zn^{2+} \rightarrow 2Cu^+$	$Cu^+_{Zn} + Cu_i$	$Cu_{2+2d}Zn_{1-d}GeSe_4$
E	Cu-poor, Zn-poor, Ge-rich	$2Cu^+ + Zn^{2+} \rightarrow Ge^{4+}$	$2V_{Cu} + Ge^{4+}_{Zn}$ or $Ge^{4+}_{Cu} + V_{Cu} + V_{Zn}$	$Cu_{2+2e}Zn_{1-e}Ge_{1+e}Se_4$
F	Cu-rich, Zn-rich, Ge-poor	$Ge^{4+} \rightarrow Zn^{2+} + 2Cu^+$	$Zn^{2+}_{Ge} + 2Cu^+_i$ or $Cu^+_{Ge} + Cu^+_I + Zn^{2+}_i$	$Cu_{2+2f}Zn_{1+f}Ge_{1-f}Se_4$
G	Cu-const., Zn-rich, Ge-poor	$Ge^{4+} \rightarrow 2Zn^{2+}$	$Zn^{2+}_{Ge} + Zn^{2+}_i$	$Cu_2Zn_{1+2g}Ge_{1-g}Se_4$
H	Cu-const., Zn-poor, Ge-rich	$2Zn^{2+} \rightarrow Ge^{4+}$	$Ge^{4+}_{Zn} + V_{Zn}$	$Cu_2Zn_{1-h}Ge_{1+1/2h}Se_4$
I	Cu-rich, Zn-const., Ge-poor	$Ge^{4+} \rightarrow 4Cu^+$	$Cu^+_{Ge} + 3Cu^+_i$	$Cu_{2(1+2i)}ZnGe_{1-i}Se_4$

J	Cu-poor, Zn-const., Ge-rich	$4Cu^{+} \rightarrow Ge^{4+}$	$Ge^{4+}_{Cu} + 3V_{Cu}$	$Cu_{2-2j}Zn_{1-j}Ge_{1+1/2j}Se_4$
K	Cu-rich, Zn/Ge=1=const.	$Zn^{2+} + Ge^{4+} \rightarrow 6Cu^{+}$	$Cu^{+}_{Zn} + Cu^{+}_{Ge} + 4Cu^{+}_{i}$	$Cu_{2+6k}Zn_{1-k}Ge_{1-k}Se_4$
L	Cu-poor, Zn/Ge=1=const.	$6Cu^{+} \rightarrow Zn^{2+} + Ge^{4+}$	$Zn^{2+}_{Cu} + Ge^{4+}_{Cu}$	$Cu_{2-2l}Zn_{1+1/3l}Ge_{1+1/3l}Se_4$

This study aims for the identification of point defect types and their correlation with the off stoichiometric composition in CZGSe. The basis for this systematic investigation are off-stoichiometric CZGSe powder samples which have been synthesized by solid state reaction according to A-, B-, C-, and D-type composition [29].

Experimental

The CZGSe powder samples have been synthesized by solid state reaction using the elements copper, zinc, germanium and selenium in high-purity (≥99.999%). Details on the synthesis route and reaction steps can be found in [30]. The elements were accurately balanced to within one milligram to form quaternary compounds with A-, B-, C- and D-type composition (c.f. Figure 2 and Table I). In order to facilitate the entire reaction of the metal pieces about 2% excess selenium was added. Additionally, in most of the synthesis runs the germanium metal pieces have been pre-ground since germanium turned out to be not fully reacted after the first synthesis step. The temperature program applied to the as-weighed samples has been adapted specifically for the substitution of Sn by Ge, and is described in Table II. Irrespective of the homogenization step, Cu-rich, Zn-poor, Ge-rich C-type samples were strongly prone to form several kesterite phases and therefore required an additional homogenization step, that is, repetition of second reaction step.

Table II. Temperature program used to synthesize CZGSe powder samples.

		T [°C]	dT/dt [K/h]	T_{hold} [h]
1st reaction step	1st heating stage	250	10	48
	2nd heating stage	450	10	48
	Final heating stage	700	10	336
	Cooling	RT	10	-
Homogenization step		Material is ground, pressed to pellets and placed into silica ampoules which are evacuated and sealed (2x done for C-type samples).		
2nd	Heating stage	700	50	336

reaction step	Cooling	RT	10	-

After the homogenization step the samples are ground to fine powder, which is required for the characterization techniques to be applied subsequently. The composition of 30 synthesized CZGSe powder samples has quantitatively been determined by an electron probe micro analyzer (EPMA) JEOL-JXA 8200 using wavelength dispersive X-ray spectroscopy (WDX) being calibrated with element standards. Line scans, each with 10 measurement spots, on numerous grains were averaged to ensure acquisition of statistically robust information on composition and homogeneity (see supplementary information Figure S1). A sample consisting of several kesterite-type phases is not suited for the in-depth structural studies by X-ray and neutron diffraction. Specifically in case of neutron diffraction, from which the site occupancy factors will eventually be derived, an accurate data analysis would not be possible in this case.

Following the homogenization steps, the samples have been characterized by powder X-ray and neutron diffraction. X-ray powder diffraction data was recorded over a 2Θ range of 10–140° with step size of 0.01313° by a PANalytical X'Pert MPD diffractometer ($\lambda_{Cu\text{-}K\alpha}$ = 1.54187 Å) using Bragg-Brentano set-up and a rotatable sample stage. However only basic structural information (e.g. lattice parameters) and quantitative phase content can be extracted since scattering powers (atomic form factor) of the isoelectronic cations Cu^{+}, Zn^{2+} and Ge^{4+} are too similar to be distinguished so that these cations cannot be differentiated by conventional X-ray diffraction. Therefore, additional neutron diffraction experiments were conducted at the fine resolution powder diffractometer E9 (λ = 1.79820 Å) [32] at BER II research reactor. The neutron diffraction patterns were collected from 15° to 140° 2Θ with a step size of 0.075°. Eventually, the obtained diffraction patterns both from X-ray as well as neutron diffraction, respectively, were analyzed using the Rietveld method [33, 34] implemented in the FullProf Suite software package [35]. As starting model for the Rietveld refinements the kesterite-type structure (s.g. $I\bar{4}$) [10-12] has been included. For the description of the peak shape profile the Thompson-Cox-Hastings pseudo-Voigt function [36] was employed, and instrumental resolution functions have been put into the refinement in order to provide more stably computation of the profile parameters.

Diffuse reflectance measurements have been performed with a hyperspectral imaging setup with a CCD camera (Allied Vision Pike F-145) coupled with a liquid crystal tunable filter (Kurios-XE2). A halogen lamp is used to illuminate the CZGSe powders. The hyperspectral stack obtained from the powders is divided over the one obtained from measuring a Spectralon SRM-99 standard to calculate the diffuse reflectance spectra.

Results and discussion

In every sample kesterite-type CZGSe was found to be the main phase. The atomic percentages of the elemental constituents obtained from quantitative electron probe micro analysis spread in the cation ratio plot show that most of the kesterite-type CZGSe can be foreseen as a mixture of two off-stoichiometry types (Figure 3). In addition to the kesterite-type phase the presence of secondary phases

in most of the samples was detected. By the combined inspection of the EPMA, XRD and ND data seven samples could be identified as single-phase, at least within the detection limit of the techniques used in this study. Single-phase samples, which contain only a kesterite-type CZGSe phase, were found mainly around the F-type line as well as between F- and I-type and close to K-type composition. ZnSe has been identified in all the samples with the exception of the single-phase powders and one powder containing only Ge as secondary phase. ZnSe along with Ge and Zn were only found in one A-B-type sample being the most Cu-poor. Likewisely far off-stoichiometric B-G-type samples exhibit small amounts of Cu-Zn alloys (Figure 3).

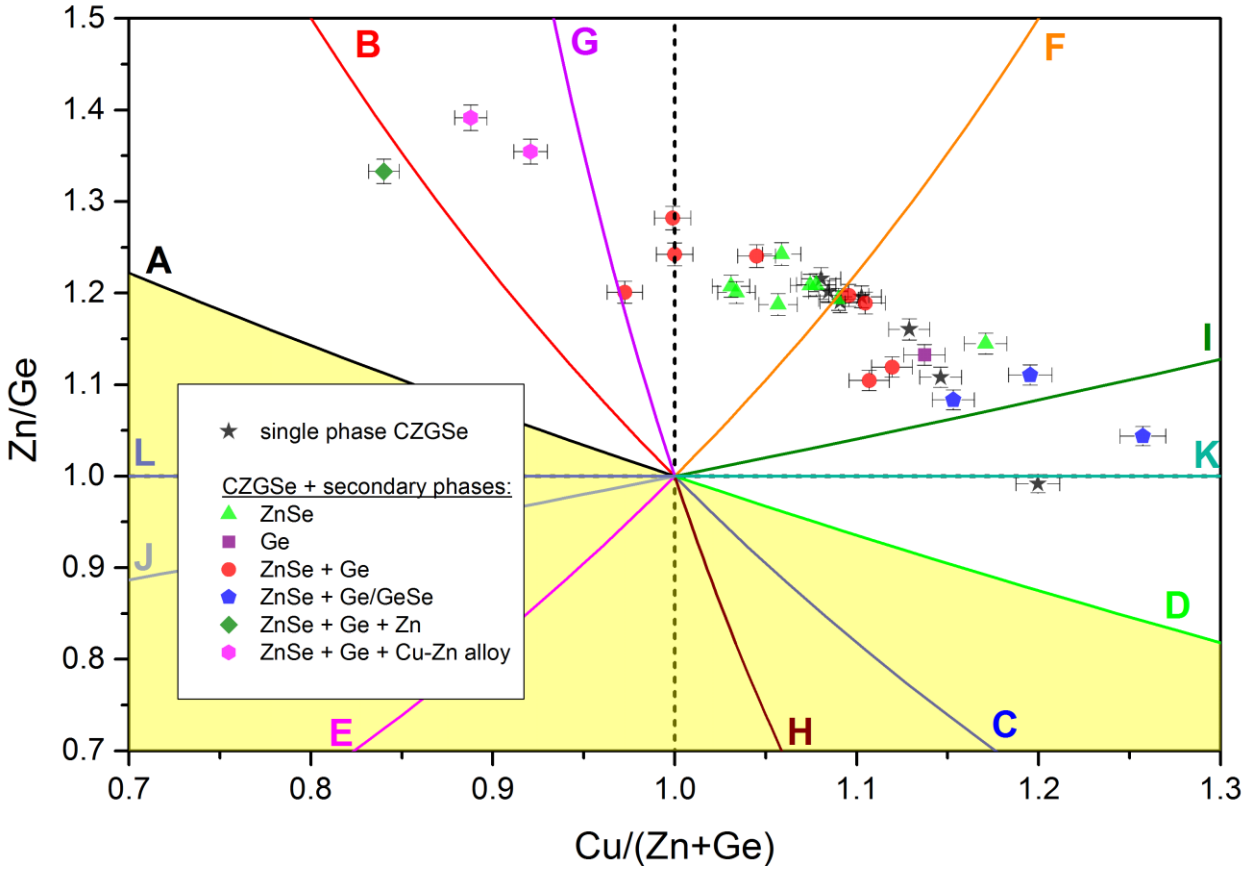

Figure 3. Cation ratio plot showing the Cu/(Zn+Ge) and Zn/Ge ratios for the kesterite-type CZGSe phase in each of the 30 synthesized samples. Solid lines indicate the course of the off-stoichiometry types A-L. Differently shaped (and colored) symbols indicate the phase content found by the various analysis techniques (i.e. EPMA, XRD, ND). Off-stoichiometry types not involved in this study are represented by shaded area.

Even though the samples were weighed-in according to A-, B-, C- and D-type progressing from the stoichiometric point Zn/Ge=Cu/(Zn+Ge)=1 towards higher off-stoichiometries along the respective type line, the final composition is fairly systematically shifted, which led to mixtures between off-stoichiometry types. That compositional shift is mainly due to the loss in Ge during the synthesis. In fact, Ge-Se binaries were found to be deposited on the internal side of the glass ampoules, and with the exception of one sample, all other samples experienced depletion in Ge (Figure 4a). Remarkably, the

deficit in Ge at its as-weighed stoichiometric coefficient ν_{Ge}=1.00, which concerns 20 out of 30 samples, show very similar values around 10 mol-%, and two samples intended to had 0.9 moles of Ge were virtually not subject to Ge loss (Figure 4a). Another striking feature is the relative overall enrichment in Cu, following quite the same trend as Ge does. Zn, on the other hand, rather exhibits an opposing trend. In the right panel of Figure 5 the remaining ν_{Ge} is shown, that is, when subtracting the Ge deficit from as-weighed ν_{Ge}. Apparently, for the given synthesis route only about 90 mol-% of Ge is incorporated (Figure 4b), regardless of the initial amount of Ge. These observations suggest that for the future development of Ge containing kesterite-type compounds, either thin films or powders, the control of the final composition is a challenging task. Further studies using different synthesis approaches and conditions should help understanding the Ge loss mechanism and its correlations to the structural and opto-electronic properties of the samples synthesized.

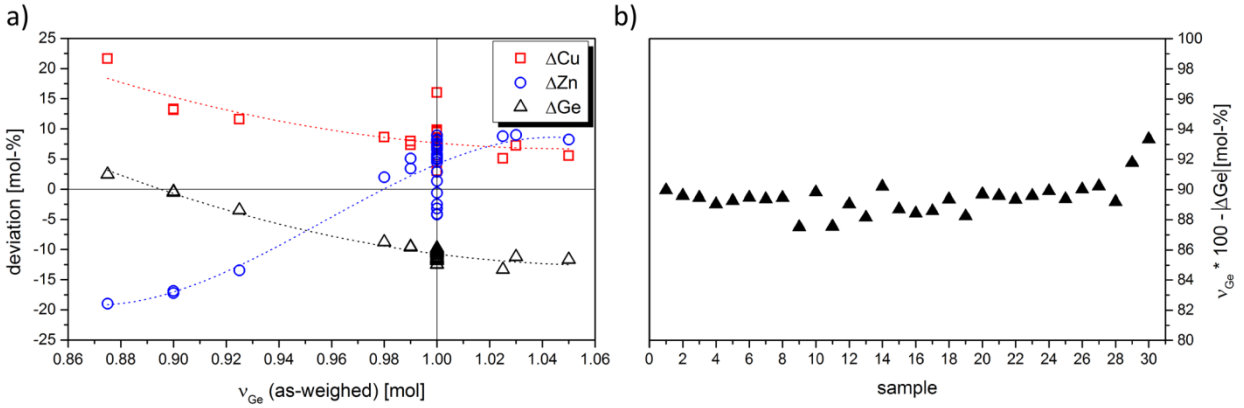

Figure 4. a) Difference between as-weighed and obtained mole percentages of the metals involved plotted against as-weighed amount of Ge. b) Irrespective of the original composition the actual mole percentage of Ge measured after the synthesis is set back to around 90 mol-%.

In order to determine the sum formula of each off-stoichiometric CZGSe phase the respective type fractions as well as the non-stoichiometric variable (i.e. a – l, c.f. Table I) have to be calculated beforehand. The non-stoichiometric variables given in the general sum formulae are calculated by forming linear equations equating known cation ratios with the corresponding stoichiometric coefficient, and are being solved for the non-stoichiometric variable (see supplementary information, Equations S1–S6). Knowing both the type fraction as well as the non-stoichiometric variable allows for the calculation of the stoichiometric coefficients of each cation, finally yielding the actual sum formula accounting for occurring point defects while maintaining the charge balance.

The lattice parameters of the phases as well as quantitative phase content were obtained from Rietveld analysis [33, 34] of the XRD data. In the Cu-poor region the lattice parameter *a* remains rather unchanged while the lattice parameter *c* steadily increases towards stoichiometric point Cu/(Zn+Ge)=1. Beyond that stoichiometric point a reverse behavior is observed with lattice parameter *a* decreasing whereas *c* turns into a plateau (Figure 5a) which, to some extent, is comparable with the observations reported for off-stoichiometric $Cu_2ZnSnSe_4$ powder samples [30]. The unit cell volume V_{uc} thus increase quite linearly from Cu-rich conditions towards stoichiometric point, culminate at slightly Cu-rich conditions at Cu/(Zn+Ge)≈1.05 and decrease linearly again towards Cu-rich direction (see supplementary information,

Figure S2). The tetragonal deformation η=c/2a, thus, is continuously decreasing, that is, approaching unity, from most Cu-poor to most Cu-rich composition (Figure 5b). Similar observations have been reported for CZTSe thin films when compared to the overall composition of the samples. The enhancement of the tetragonal deformation has been associated with an increase of the bandgap of the material and subsequently to an increase of the open circuit voltage (V_{OC}) of the solar cells produced with them [37]. Additionally, due to crystal field splitting and the tetragonal deformation, the valence band splits into two sub-bands: a non-degenerate Γ_{4v} and a doubly degenerate Γ_{5v} band. For c/2a ratios below 1, it has been predicted that the Γ_{4v} band is higher in energy than the Γ_{5v} band [38]. The energy difference between these two bands increases with increasing deviation from 1. Variations on the tetragonal deformation parameter can alter significantly the electronic transport properties of kesterite-type compounds and can be used to tune the thermoelectric properties of these materials [39].

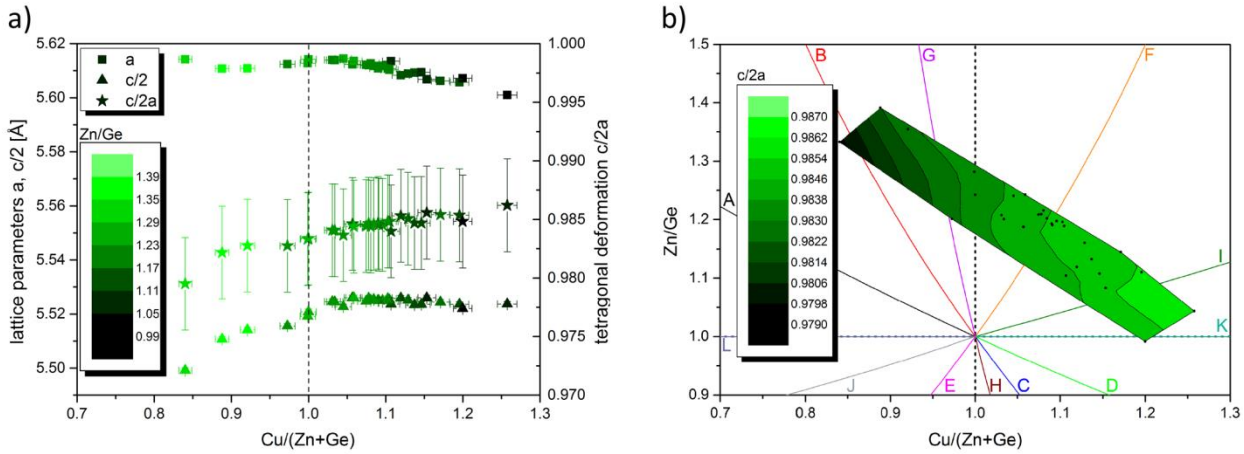

Figure 5. a) Lattice parameters and tetragonal deformation in dependence of Cu/(Zn+Ge). b) Tetragonal deformation as contour plot versus cation ratios.

Neutron diffraction experiments were conducted in order to determine the distribution of cations within the crystal structure which, in turn, is used to estimate both the point defect species as well as their concentration. Since the contrast in neutron scattering lengths of the cations b_j (Cu=7.718 fm, Zn=5.680 fm, Ge=8.185 fm) is sufficiently strong and, unlike X-ray diffraction, scattering power is not a function of 2θ, neutron diffraction provides valuable data for refining site specific anisotropic temperature factors (B_{aniso}) and site occupancy factors (sof). The sof is refined for each cation site (Cu-2a, Cu-2c, Zn-2d, Ge-2b) and gives the basis for the experimentally deduced average neutron scattering lengths of the cation sites:

$$\bar{b}_j^{exp} = sof_j \cdot b_j. \qquad (7)$$

Here j stands for the Wyckoff position which is 2a, 2b, 2c and 2d. If sof≠1, the average neutron scattering length of that particular Wyckoff position does differ from the neutron scattering length of the corresponding cation, meaning that a certain fraction of that site is occupied by another cation or is even partly vacant. In accordance with the given composition and the related off-stoichiometry types the

cation distribution is modeled by assuming the according point defects on the concerning Wyckoff position:

$$\bar{b}_j^{mod} = X_j b_x + Y_j b_y + V_j. \qquad (8)$$

Here V stands for vacancies, where X and Y are cation fractions, e. g. the cation which occupies this site according to the kesterite-type structure and another cation which then forms an antisite defect. The modeled cation distribution can be numerically solved such that the difference between experimental average neutron scattering length and the modeled one becomes as minimal as possible. This model has to fulfill the compositional restrains and those of the type specific point defects and is ultimately constrained by the error bars of the experimental average neutron scattering lengths. The errors of the experimental average neutron scattering lengths are given by the errors of the site occupancy factors sof obtained by the Rietveld refinement of the neutron diffraction data. That modeling of cation distribution has been applied to 28 out of 30 off-stoichiometric CZGSe powder samples, comprising one A/B-type, one K/D-type, two B/G-type, 11 G/F-type, and 13 F/I-type off-stoichiometric kesterite. The neutron diffraction patterns of the remaining two samples were too much deteriorated by peak overlap leading to poor results with respect to temperature factors as well as site occupancy factors and, thus, have not been included. The experimental average neutron scattering lengths successfully deduced from Rietveld analysis of neutron diffraction data are compiled in Figure 6a, together with the modeled average neutron scattering lengths. The occupancies of the cation sites by different cations and vacancies can be established from the modeled average neutron scattering lengths (Figure 6b).

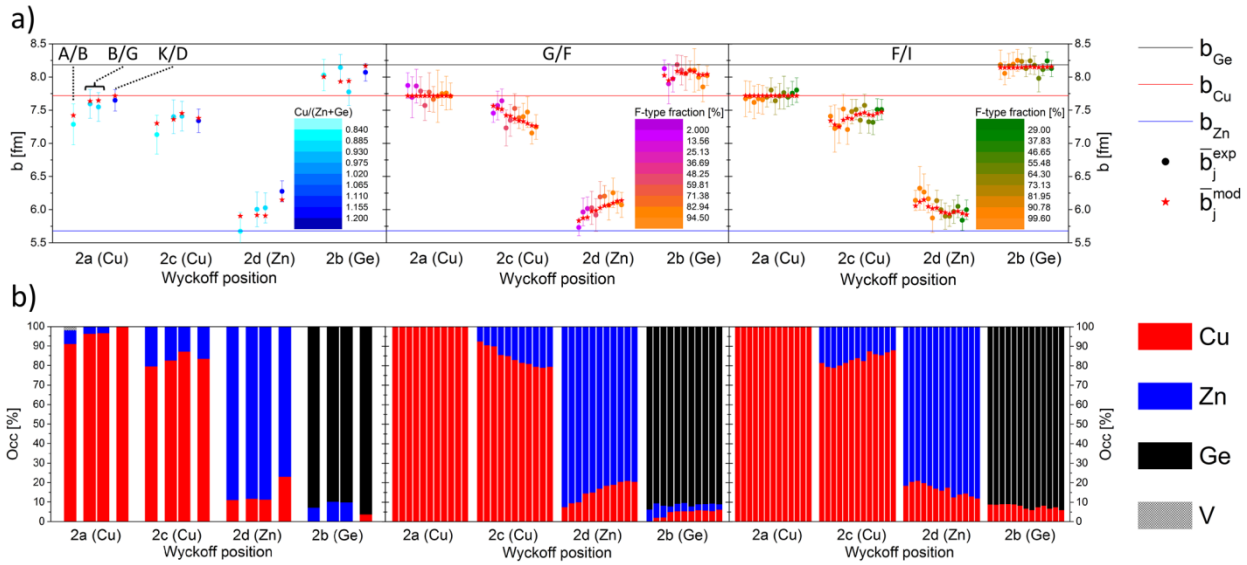

Figure 6. Results from Rietveld analysis of neutron diffraction data of off-stoichiometric CZGSe powder samples showing a) experimental average neutron scattering length *b* vs. modeled average neutron scattering length and b) corresponding occupancies (*Occ)* of the cation sites.

With regard to Figure 6 it is obvious that in Cu-poor CZGSe (A/B- and B/G-type) the 2a and 2c Wyckoff positions are partly occupied by Zn, giving rise to Zn_{Cu} antisites and Cu/Zn disorder between 2c and 2d Wyckoff positions. On the contrary, from slightly Cu-poor regime to the highly Cu-rich compositions (i.e.

G/F-, F/I-, K/D-type) the Cu/Zn disorder is the predominant defect. The overall deficiency of Ge is giving rise to Zn_{Ge} and Cu_{Ge} antisite defects all over the compositional range.

The point defect concentration can be obtained by considering the unit cell volume, which has been calculated from the lattice parameters determined by Rietveld analysis of the XRD data, and the fractional occupancy of the Wyckoff positions being modeled for the point defects. However, cations being on interstitial positions (i.e. Cu_i, Zn_i), self-evidently, cannot be treated like cations occupying regular Wyckoff positions given by symmetry but the cations remaining from the modeled distribution are considered as interstitials instead. The concentration of the different structural point defect types (vacancies, antisites, interstitials) is mainly of the order 10^{19} to 10^{21} cm^{-3} (Figure 7), cumulatively corresponding to one point defect per about every third to fourth unit cell.

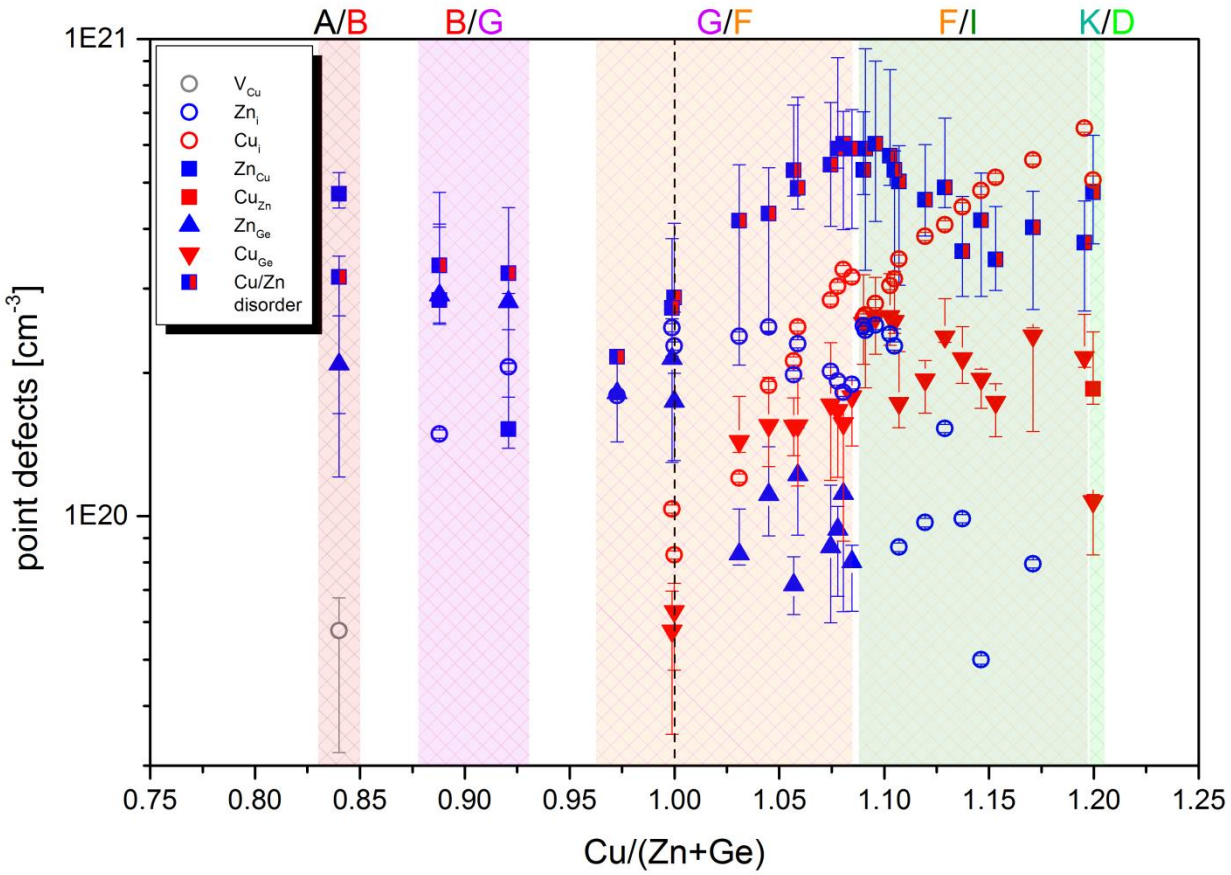

Figure 7. Concentration of type specific point defects and Cu/Zn disorder defect in off-stoichiometric kesterite-type CZGSe.

The Cu/Zn disorder is the defect being in common for all samples. A minimum in Cu/Zn disorder is observed in the slightly Cu-poor regime close to the stoichiometric point (Cu/(Zn+Ge)=1) which coincides with the minimum in total point defect concentration (see supplementary information Figure S3). In Cu-poor samples a high concentration of Zn_{Cu} and Zn_{Ge} antisites was found, and as the vast majority of the samples are Zn-rich the Zn_i interstitial defect is present over a wide compositional range, with declining concentration at moderate Cu-rich conditions and finally ceasing at the onset of K/D-type composition. From stoichiometric point towards slightly Cu-rich conditions the concentration of Cu_i interstitials along

with Cu_{Ge} antisites are steeply increasing. While the Cu_i defects continue following this trend the concentration of Cu_{Ge} antisites only smoothly increases towards highly Cu-rich conditions, and even decrease when reaching the K/D-type composition where Cu is additionally consumed to form Cu_{Zn} antisites.

According to the cationic radii Cu^{+}=0.60 Å, Zn^{2+}=0.74 Å, and Ge^{4+}=0.39 Å [40] compositional variations should be readily recognized by correspondingly altered lattice parameters. The impact of changing composition on unit cell metrics however is difficult to be evaluated as its effect is superimposed by these defect complexes both with varying concentration and different defect types, respectively. The increase in unit cell volumes from Cu-poor conditions to slightly Cu-rich regime might be due to the fact that Cu content is increasing faster than the Zn content does decrease. That assumption seems to be valid until Cu/(Zn+Ge)≈1.05 where the onset of the decrease in lattice parameter *a* and, consequently, the drop in unit cell volume is observed, although Cu and Zn contents do change in the same manner as in the Cu-poor region. However, the rapid decrease in unit cell volumes to some extent correlates with the decrease in Zn_i interstitial concentration, though the Cu_i interstitial concentration is further steeply increasing but lacking the ability to counteract the unit cell shrinkage due to its smaller radius. Germanium, on the other hand, can be basically ruled out to have a significant impact on the evolution of unit cell metrics as the germanium content remains fairly constant (c.f. Figure 5a and supplementary information Figure S4) and as it is solely found on its designated position (c.f. Figure 6).

Diffuse reflectance hyperspectral imaging has been used to evaluate the bandgap of the powders synthesized. Tauc plots generated with the Kubelka-Munk function were used for the bandgap calculation (Figure S5) [41, 42]. A gradual bandgap widening has been observed as the Cu content decreases on the powders (Figure 8). An increase of up to 40 meV is observed in Kesterite-type CZGSe with Cu/(Zn+Ge)∼1 (1.36 eV) to Cu/(Zn+Ge)∼0.84 (1.4 eV). A similar bandgap widening has also been observed in CZTSe thin films as the Cu content decreases in their overall composition [37, 43]. This increase in bandgap with decreasing Cu content is attributed to a downshift of the valence band maximum which is mainly formed by antibonding states from the hybridization of Cu-d and Se-p orbitals [44, 45]. An increase of reflectance below the bandgap of all the powders with Cu/(Zn+Ge)>1 could not be observed, limiting the bandgap calculation just to Cu-poor samples. All the Cu-rich samples have shown high concentration of Cu_{Ge} point defects (Figure 7), which by analogy with Cu_{Sn} have been predicted to introduce deep states in the kesterite-type semiconductors that are detrimental for the solar cell performance [46]. These deep states can induce sub-bandgap absorption explaining why it was not possible to observe any increase in the reflectance in these samples. In addition, this also suggests that CZGSe with Cu-poor composition should also be preferred for the fabrication of solar cells as observed for CZTSe [37, 46, 47].

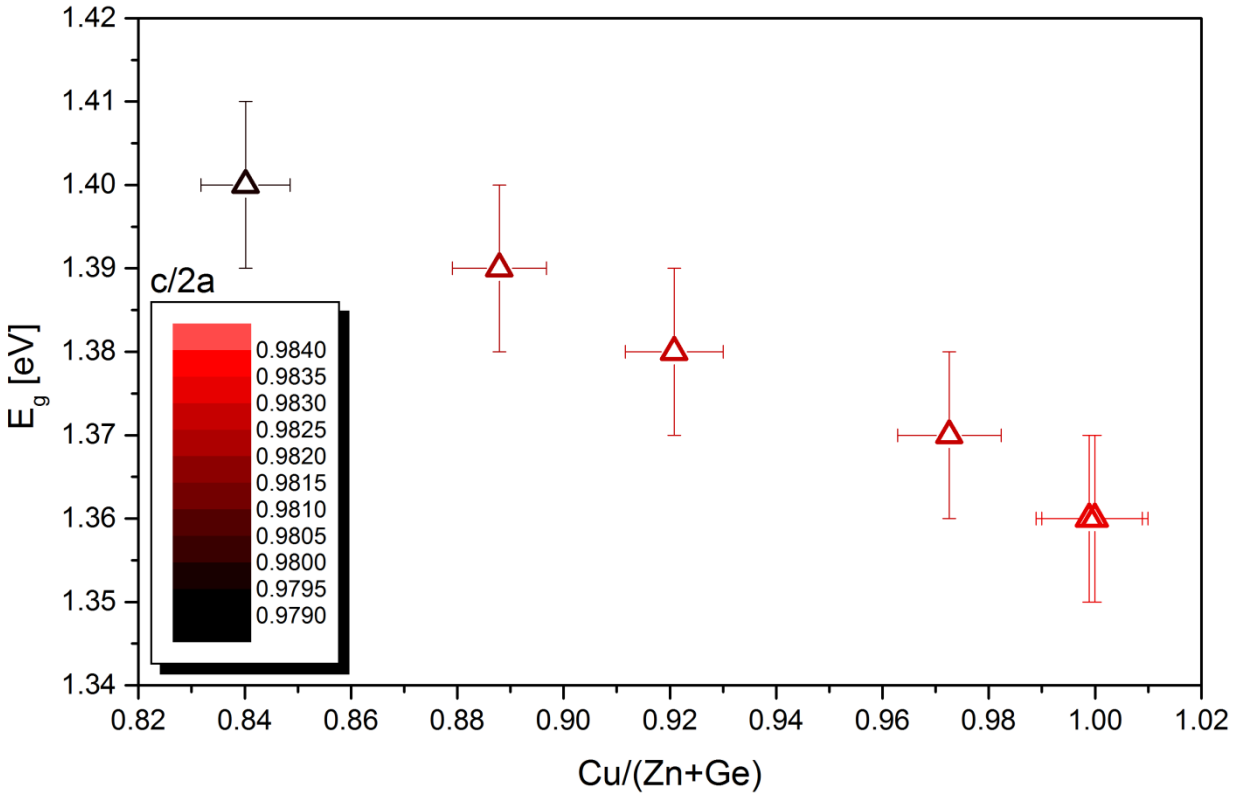

Figure 8. Bandgap energy of off-stoichiometric kesterite-type CZGSe in dependence on Cu/(Zn+Ge) cation ratio.

Conclusion

Off-stoichiometric CZGSe powder samples have successfully been synthesized by solid state reaction. The formation of single-phase CZGSe samples however seems more likely to happen in the Cu-rich regime. From neutron diffraction data the cation distribution in the kesterite-type structure could be established applying the average neutron scattering length analysis method and the occurring defect types and their correlation with composition have been successfully investigated. While compositional changes are clearly reflected by the tetragonal deformation *c/2a*, the lattice parameters *a*, *c* seem differently responding to changing point defect types and concentration, respectively. The Cu_{Ge} antisite defect which is known to greatly deteriorate the opto-electronic properties starts to appear at Cu/(Zn+Ge)≈1, and its concentration generally increases towards more Cu-rich conditions. Diffuse reflectance measurements demonstrate that the energy of the bandgap increases in off-stoichiometric kesterite-type CZGSe with decreasing Cu/(Zn+Ge).

Acknowledgement

This research was supported by the H2020 programme under the project STARCELLS (H2020-NMBP-03-2016-720907). Financial support from HZB Graduate School “Materials for Solar Energy Conversion” (MatSEC) is highly appreciated.

References

1. L. Guen and W. Glaunsinger, *Journal of Solid State Chemistry*, 1980, 35, 10-21.
2. J. Shay, S. Wagner and H. Kasper, *Applied Physics Letters*, 1975, 27, 89-90.
3. N. Nakayama and K. Ito, *Applied Surface Science*, 1996, 92, 171-175.
4. H. Katagiri, N. Sasaguchi, S. Hando, S. Hoshino, J. Ohashi and T. Yokota, *Solar Energy Materials and Solar Cells*, 1997, 49, 407-414.
5. W. Wang, M. T. Winkler, O. Gunawan, T. Gokmen, T. K. Todorov, Y. Zhu and D. B. Mitzi, *Advanced Energy Materials*, 2014, 4.
6. G. Kühn and H. Neumann, *Zeitschrift für Chemie*, 1987, 27, 197-206.
7. M. Neuschitzer, J. Marquez, S. Giraldo, M. Dimitrievska, M. Placidi, I. Forbes, V. Izquierdo-Roca, A. Pérez-Rodriguez and E. Saucedo, *The Journal of Physical Chemistry C*, 2016, 120, 9661-9670.
8. C. J. Hages, N. J. Carter, R. Agrawal and T. Unold, *Journal of Applied Physics*, 2014, 115, 234504.
9. B. Pamplin, *Progress in Crystal Growth and Characterization*, 1980, 3, 179-192.
10. S. R. Hall, J. T. Szymanski and J. M. Stewart, *The Canadian Mineralogist*, 1978, 16, 131-137.
11. S. Schorr, *Solar Energy Materials and Solar Cells*, 2011, 95, 1482-1488.
12. S. Schorr, *Thin Solid Films*, 2007, 515, 5985-5991.
13. W. L. Bragg and E. J. Williams, *Proceedings of the Royal Society of London. Series A*, 1934, 145, 699-730.
14. J. J. S. Scragg, L. Choubrac, A. Lafond, T. Ericson and C. Platzer-Björkman, *Applied Physics Letters*, 2014, 104, -.
15. D. M. Többens, G. Gurieva, S. Levcenko, T. Unold and S. Schorr, *physica status solidi (b)*, 2016, 253, 1890-1897.
16. G. Gurieva, L. E. V. Rios, A. Franz, P. Whitfield and S. Schorr, *Journal of Applied Physics*, 2018, 123, 161519.
17. M. J. Romero, H. Du, G. Teeter, Y. Yan and M. M. Al-Jassim, *Phys. Rev. B*, 2011, 84, 165324-165321--165324-165325-165324.
18. U. Rau and J. Werner, *Applied physics letters*, 2004, 84, 3735-3737.
19. T. Gokmen, O. Gunawan, T. K. Todorov and D. B. Mitzi, *Applied Physics Letters*, 2013, 103, 103506.
20. G. Rey, A. Redinger, J. Sendler, T. P. Weiss, M. Thevenin, M. Guennou, B. El Adib and S. Siebentritt, *Applied Physics Letters*, 2014, 105, 112106.
21. T. Gershon, K. Sardashti, O. Gunawan, R. Mankad, S. Singh, Y. S. Lee, J. A. Ott, A. Kummel and R. Haight, *Advanced Energy Materials*, 2016, 6.
22. J. Márquez, H. Stange, C. J. Hages, N. Schaefer, S. Levcenko, S. Giraldo, E. Saucedo, K. Schwarzburg, D. Abou-Ras, A. Redinger, M. Klaus, C. Genzel, T. Unold and R. Mainz, *Chemistry of Materials*, 2017, DOI: 10.1021/acs.chemmater.7b03416.
23. K. Maeda and K. Domen, *The Journal of Physical Chemistry Letters*, 2010, 1, 2655-2661.
24. S. Chen, A. Walsh, J.-H. Yang, X. G. Gong, L. Sun, P.-X. Yang, J.-H. Chu and S.-H. Wei, *Physical Review B*, 2011, 83, 125201.
25. S. Chen, X. G. Gong, A. Walsh and S.-H. Wei, *Phys. Rev. B*, 2009, 79, 165211-165211--165211-165210-165211.
26. W. Shockley and H. J. Queisser, *Journal of applied physics*, 1961, 32, 510-519.
27. A. Ennaoui, M. Lux-Steiner, A. Weber, D. Abou-Ras, I. Kötschau, H.-W. Schock, R. Schurr, A. Hölzing, S. Jost and R. Hock, *Thin Solid Films*, 2009, 517, 2511-2514.
28. H. Katagiri, K. Jimbo, W. S. Maw, K. Oishi, M. Yamazaki, H. Araki and A. Takeuchi, *Thin Solid Films*, 2009, 517, 2455-2460.

29. A. Lafond, L. Choubrac, C. Guillot-Deudon, P. Deniard and S. Jobic, *Zeitschrift für Anorganische und Allgemeine Chemie*, 2012, 638, 2571-2577.
30. L. E. V. Rios, K. Neldner, G. Gurieva and S. Schorr, *Journal of Alloys and Compounds*, 2015.
31. P. Schöppe, G. Gurieva, S. Giraldo, G. Martínez-Criado, C. Ronning, E. Saucedo, S. Schorr and C. S. Schnohr, *Applied Physics Letters*, 2017, 110, 043901.
32. A. Franz and A. Hoser, *Journal of large-scale research facilities JLSRF*, 2017, 3, 103.
33. H. M. Rietveld, *Acta Crystallographica*, 1967, 22, 151-152.
34. H. M. Rietveld, *Journal of Applied Crystallography*, 1969, 2, 65-71.
35. J. Rodriguez-Carvajal, 2001.
36. P. Thompson, D. Cox and J. Hastings, *Journal of Applied Crystallography*, 1987, 20, 79-83.
37. J. Márquez, M. Neuschitzer, M. Dimitrievska, R. Gunder, S. Haass, M. Werner, Y. Romanyuk, S. Schorr, N. Pearsall and I. Forbes, *Solar Energy Materials and Solar Cells*, 2016, 144, 579-585.
38. J. Zhang, R. Liu, N. Cheng, Y. Zhang, J. Yang, C. Uher, X. Shi, L. Chen and W. Zhang, *Advanced Materials*, 2014, 26, 3848-3853.
39. W. G. Zeier, H. Zhu, Z. M. Gibbs, G. Ceder, W. Tremel and G. J. Snyder, *Journal of Materials Chemistry C*, 2014, 2, 10189-10194.
40. R. D. Shannon, *Acta crystallographica section A: crystal physics, diffraction, theoretical and general crystallography*, 1976, 32, 751-767.
41. P. Kubelka, *Josa*, 1948, 38, 448-457.
42. A. Murphy, *Solar Energy Materials and Solar Cells*, 2007, 91, 1326-1337.
43. M. V. Yakushev, M. A. Sulimov, J. Márquez-Prieto, I. Forbes, J. Krustok, P. R. Edwards, V. D. Zhivulko, O. M. Borodavchenko, A. V. Mudryi and R. W. Martin, *Solar Energy Materials and Solar Cells*, 2017, 168, 69-77.
44. S. Chen, X. G. Gong, A. Walsh and S.-H. Wei, *Applied Physics Letters*, 2009, 94, 041903-041901--041903-041903-041903.
45. S. Botti, D. Kammerlander and M. A. L. Marques, *Applied Physics Letters*, 2011, 98, 241915-241911--241915-241913-241915.
46. S. Chen, A. Walsh, X. G. Gong and S. H. Wei, *Advanced Materials*, 2013, 25, 1522-1539.
47. A. Collord and H. Hillhouse, *Chemistry of Materials*, 2016, 28, 2067-2073.